Electrochemical characterization and surface analysis of bulk amorphous alloys in aqueous solutions at different *p*H

R. Schennach
Gill Chair of Chemistry and Chemical Engineering Research Group, Lamar University, Beaumont, Texas and Department of Physics, Texas A&M University, College Station, Texas

T. Grady
Department of Chemistry, Prairie View A&M University, Prairie View, Texas

D. G. Naugle
Department of Physics, Texas A&M University, College Station, Texas

H. McWhinney
Department of Chemistry, Prairie View A&M University, Prairie View, Texas

C. C. Hays and W. L. Johnson
Division of Engineering and Applied Science 138-78, California Institute of Technology, Pasadena, California

D. L. Cocke[a)]
Gill Chair of Chemistry and Chemical Engineering Research Group, Lamar University, Beaumont, Texas

(Received 1 September 2000; accepted 2 May 2001)

Bulk amorphous alloys are a new class of materials with a variety of characteristics that make them useful for applications in aqueous environments. While some bulk amorphous metals show increased corrosion resistance, there is still a lack of fundamental electrochemical studies of these materials. Two different compositions of BeCuNiTiZr bulk amorphous alloys have been studied at *p*H 5, 7, and 10 using cyclic voltammetry (CV), x-ray photoelectron spectroscopy (XPS), depth profiling methods, and optical microscopy. While XPS is used to determine the composition of the resulting oxide films, the CV curves and optical micrographs are compared to pinpoint differences in the corrosion resistance of the amorphous multicomponent alloys. The effect of the amorphicity, multicomponent structure and the presence of elements with widely varying interfacial reactivities on the oxidation process and on the corrosion resistance of the alloys, are discussed with the desire to provide some electrochemical background for the expected wide spread use of bulk amorphous alloys. [DOI: 10.1116/1.1380719]

I. INTRODUCTION

Amorphous metals have long been electrochemically studied because of their unusually high resistance to corrosion.[1] The need for electrochemical research has recently been increasing because their compositional complexity has been increasing to enhance their mechanical properties and resistance to crystallization.[2,3] A number of multicomponent strongly glass-forming metallic alloys represented by the Zr–Ti–Cu–Ni–Be,[4] Zr–Cu–Ni–Al,[5] and Pd–Cu–Ni–P (Ref. 6) systems are now being produced in bulk form. This has allowed structural components to be produced and has heightened interest in their electrochemical and corrosion properties.[3] While there are a number of studies on the crystallization and phase separation properties of these alloys,[7–11] there is a paucity of both fundamental and applied studies of their interfacial characteristics and surface reactivities. The Zr–Ti–Cu–Ni–Be bulk amorphous alloys examined in this study crystallize at temperatures above about 650 K. This makes them particularly interesting candidates for structural applications and some have already been commercialized as golf club heads.[12] Since structural components experience oxidative conditions in many different environments and in many electrochemical situations, bulk amorphous alloys used for these purposes will need to be electrochemically examined. This makes the oxidation process and the corrosion resistance of these bulk amorphous alloys an important field of research. Oxidation and corrosion of alloys are linked, because oxidation can be viewed as an electrochemical process.

Oxidation of alloys depends on the alloy composition as well as on the properties of the individual components. It has been shown for several binary alloys[13–19] that a modified Cabrera Mott model[17] can be used to predict the structure of the oxide film during thermal and electrochemical oxidation. The modified Cabrera Mott model leads to the following equation for the potential ($\Delta\Phi$) that drives the oxidation process:[17]

$$\Delta\Phi = \frac{-\Delta G^0_{f_{M_1}}}{2be^-} + \frac{kT}{2be^-}\ln\left[\frac{(2be^-)^b N_S^b a_{O_2}^{b/2} a_{M_1}^a X^b}{kT\epsilon^b \epsilon_0^b a_{M_1^{2b/a^+}}^a}\right] + \frac{-\Delta G^0_{f_{M_2}}}{2de^-} + \frac{kT}{2de^-}\ln\left[\frac{(2de^-)^d N_S^d a_{O_2}^{d/2} a_{M_2}^c X^d}{kT\epsilon^d \epsilon_0^d a_{M_2^{2d/c^+}}^c}\right] + \cdots . \quad (1)$$

a)Author to whom correspondence should be addressed; electronic mail: cockedl@hal.lamar.edu

The terms in Eq. (1) are the following: the free energies of oxide formation per mole of O^{2-} $(-\Delta G^0_{f_{M_x}})$ for the alloy components M_1 and M_2; the stoichiometric factors from the oxidation reactions (a, b, c, and d), the oxygen, metal, and metal ion activities (a_x); the number of surface O^{2-} (N_s); the oxide layer thickness (X); the absolute temperature (T); the Boltzmann constant (k); the relative dielectric constant (ϵ); and the dielectric constant in vacuum (ϵ_0).[17] From Eq. (1) it can be seen that the potential necessary to oxidize a specific component of an alloy mainly depends on the free energy of oxide formation on a per mole of oxygen basis, leading to an easy way to predict which components are going to oxidize first.

The modified Cabrera Mott model has been shown to predict the structure of oxide films grown on clean metal surfaces in the gas phase using oxygen gas. In an effort to compare thermal oxidation, plasma oxidation, and anodic oxidation, we have shown that the modified Cabrera Mott model can be used for all three oxidation methods.[20] In the case of anodic oxidation, the model only holds for small voltages (<4 V), reached by linear sweep voltammetry with a scan rate of about $10-20\,\mathrm{mV\,s^{-1}}$. Under conditions usually used in anodic film growth ($\sim 50-150$ V for several minutes) there is a strong influence of possible anodic dissolution, which is accelerated by the formation of soluble metal anion complexes. Anodic dissolution of one or more components of the amorphous metals used in this study under the conditions applied cannot be ruled out. On the other hand, there was no evidence of anodic dissolution for the alloys used in Ref. 13 under similar conditions.

In this article, we present data on the corrosion resistance of two compositions of amorphous alloys consisting of Be, Cu, Ni, Ti, and Zr under anodic oxidation conditions in three solutions with different pH. The electrochemical oxidation of two amorphous alloys will also be used to explore the validity of the modified Cabrera Mott model for more complex alloys.

II. EXPERIMENT

The amorphous alloys $(Zr_{80}Ti_{20})_{55}(Ni_{51}Cu_{49})_{20}Be_{25}$ (referred to as alloy 1 in this work) and $(Zr_{67}Ti_{33})_{55}[(Ni_{45}Cu_{55})_{50}Be_{50}]_{45}$ (referred to as alloy 2 in this work) were made from the pure metals by arc melting under argon atmosphere or by injection casting under vacuum. The details of these methods are described elsewhere.[8] The samples were abrasively cleaned and polished and a minimum time was maintained to place the samples in the solutions at reducing potentials.

Anodic oxidation of the amorphous alloys was done at pH values of 5, 7, and 10 using a Solartron 1280 Potentiostat with a Ag/AgCl reference electrode and a Pt auxiliary electrode. The voltages given in this article are against this reference. The voltage was scanned from -1.5 V up to 3.5 V. The scan rate was $10\,\mathrm{mV\,s^{-1}}$. The samples were held at the initial reducing potential for 20 min before each CV and anodic film growth to give a constant beginning surface condition and to remove any air-formed films. Halide-free, buffer solutions of pH 5, 7, and 10, obtained from Fischer Scientific as: potassium biphthalate–sodium hydroxide; potassium phosphate monobasic–sodium hydroxide, and potassium carbonate–potassium borate–potassium hydroxide systems, were used to maintain a constant pH during anodic oxidation. Although the anionic species in the solutions differ for the different pH values and might be expected to influence the anodic films by altering growth patterns and possibly be slightly incorporated into the films, these affects were considered minor to avoiding the presence of aggressive halide anions. Anion effects are currently being studied on bulk amorphous alloys and will be reported later. Solutions were adjusted to the constant same ionic strengths. The alloys were initially polarized at hydrogen evolution potentials, by starting the anodic sweep at -1.5 V. Prolonged reductions of the surfaces (at greater times than 20 min) were not used since minimum times were taken to place the samples into the solutions and the known resistance of amorphous alloys to oxidation would limit native oxide growth. No precipitation of any metal hydroxides were observed in the voltage and pH ranges studied.

The electrochemically oxidized samples and untreated samples, as references, were analyzed by x-ray photoelectron spectroscopy using a Perkin Elmer PHI 5600 ESCA system. The background pressure in the XPS was in the 10^{-9} Torr range. A Mg anode was used, and the carbon signal from adventitious carbon (284.6 eV) was used for calibrating the XPS. A voltage of 15 kV and an emission current of 23 mA were used for all experiments. The analyzed surface area was $0.4\,\mathrm{mm^2}$.

XPS depth profiles were recorded using an argon pressure of 1×10^{-2} mP and an acceleration voltage of 4 kV. The argon ion beam was rastered over a surface area of $1\,\mathrm{mm^2}$. Depth profiles were acquired in a sequence of XPS measurements of the Be $1s$, Cu $2p$, Ni $2p$, O $1s$, Ti $2p$, and Zr $3d$ signals followed by argon sputtering for 30 s, up to a total sputter time of 4 min. Surface concentrations were determined using the Perkin Elmer software. The peak heights of all elements detected and their respective sensitivity factors were used to give surface concentrations in atomic %.

The surfaces were examined using an optical microscope with a magnification of $\times 50$. Pictures were taken with the microscope at the same magnification using a green filter and black and white Polaroid (Polapan 52) film with ISO 400/27° and an exposure time of 2 s.

III. RESULTS AND DISCUSSION

The electrochemical oxidation can only be done *ex situ* of the XPS system. Therefore, we compare the oxide films formed at different pH values to the native oxide formed on the amorphous alloy samples. We refer to the native oxide for both compositions as reference. Figure 1 shows the anodic current density as a function of the applied potential. At pH 10 both alloys show a passive film in the potential region between -0.27 V (alloy 1) -0.16 V (alloy 2) and 1.05 V [Figs. 1(e) and 1(f)]. The lower potential indicates the end of the formation of the passive film right after the slight in-

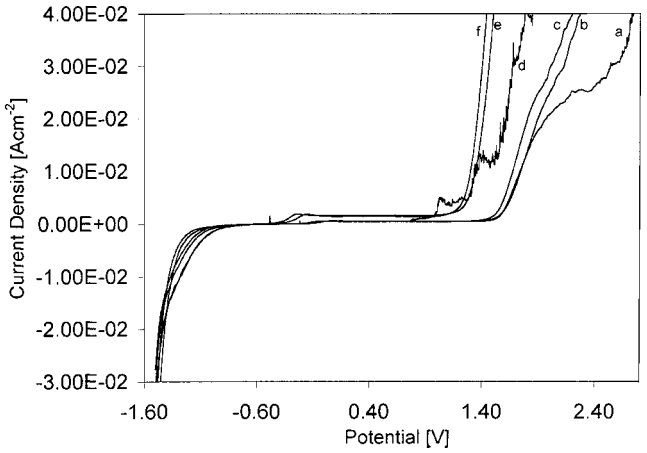

FIG. 1. Cyclic voltammogram of alloy 1 and alloy 2 at different *p*H values. (a) alloy 2 *p*H 5, (b) alloy 1 *p*H 7, (c) alloy 2 *p*H 7, (d) alloy1 *p*H 5, (e) alloy 1 *p*H 10, and (f) alloy 2 *p*H 10.

crease in the anodic current (Fig. 1) and the higher potential indicates the beginning of passive film breakdown, where the anodic current starts to increase significantly, indicating the onset of oxide growth. No pitting was observed on the surface at *p*H 10 by optical microscopy. At *p*H 7 the passive region spans from -0.02 up to 1.40 V for both alloys [Figs. 1(b) and 1(c)]. The shift in the potential of passive film breakdown to a more positive potential indicates increased corrosion resistance for both alloys at *p*H 7. Again, no pitting was observed at the surfaces of the alloys by optical microscopy. At *p*H 5 there is a significant difference between the two alloys. Alloy 1 shows a passive region between -0.02 and 0.76 V, indicating a sharply decreased corrosion resistance in acidic solution [Fig. 1(d)]. In this case, the breakdown of the passive film is associated with severe pitting of the surface, as shown in the optical micrograph in Fig. 2(b). Alloy 2 has the same passive region at *p*H 5 as at *p*H 7 [Fig. 1(a)], but the breakdown of the passive film is associated with pitting on the surface [Fig. 2(c)]. The pitting observed for both alloys at *p*H 5 may be linked with selective dissolution of one of the alloy components. Although the two alloy compositions show a similar corrosion behavior at *p*H 7 and 10, there is a significant difference at *p*H 5, with alloy 2 showing the better corrosion resistance.

From the modified Cabrera Mott model one would expect the native oxide to contain mainly BeO, ZrO_2, and some TiO. The corresponding free energies of formation in a per mole of oxygen basis[21] are $-580.1\,\mathrm{kJ\,mol^{-1}}$ for BeO, $-521.4\,\mathrm{kJ\,mol^{-1}}$ for ZrO_2, $-495.0\,\mathrm{kJ\,mol^{-1}}$ for TiO, $-478.1\,\mathrm{kJ\,mol^{-1}}$ for Ti_2O_3, $-444.8\,\mathrm{kJ\,mol^{-1}}$ for TiO_2, $-292.0\,\mathrm{kJ\,mol^{-1}}$ for Cu_2O, $-244.3\,\mathrm{kJ\,mol^{-1}}$ for NiO, and $-129.7\,\mathrm{kJ\,mol^{-1}}$ for CuO. The depth profiles of the two al-

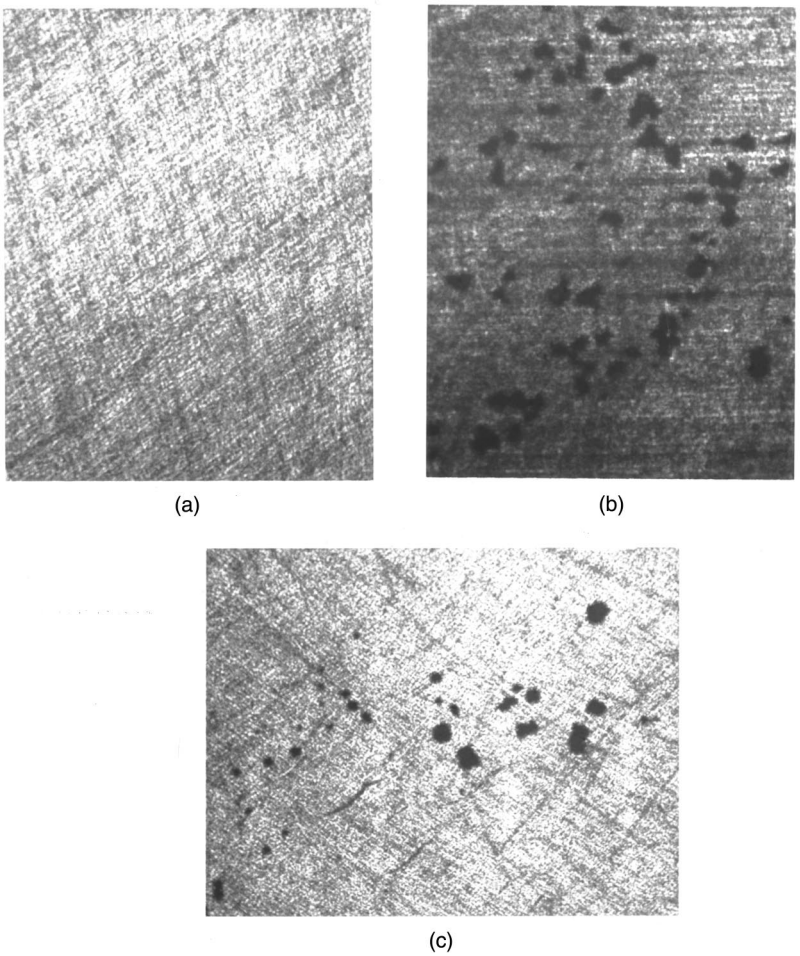

FIG. 2. Optical micrographs of (a) alloy 1 as polished, (b) alloy 1 anodically oxidized at *p*H 5, (c) alloy 2 anodically oxidized at *p*H 5. Magnification ×50.

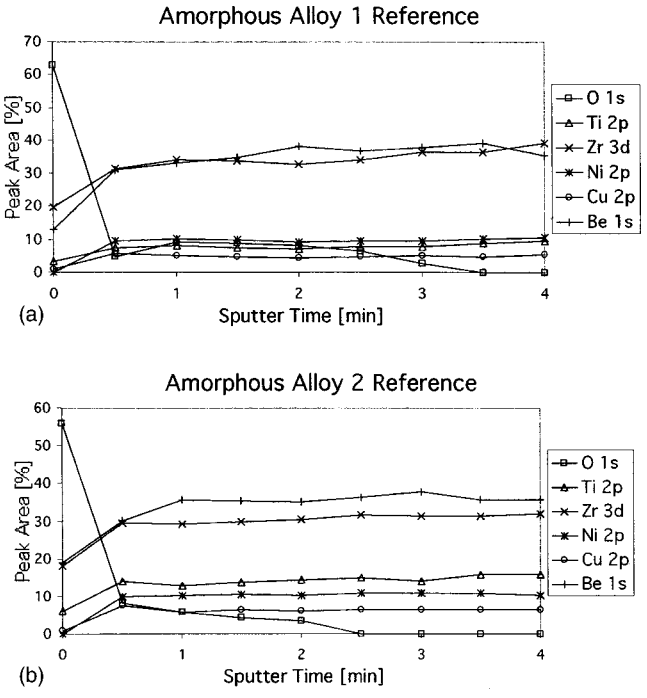

FIG. 3. XPS depth profiles of (a) alloy 1 and (b) alloy 2 before anodic oxidation.

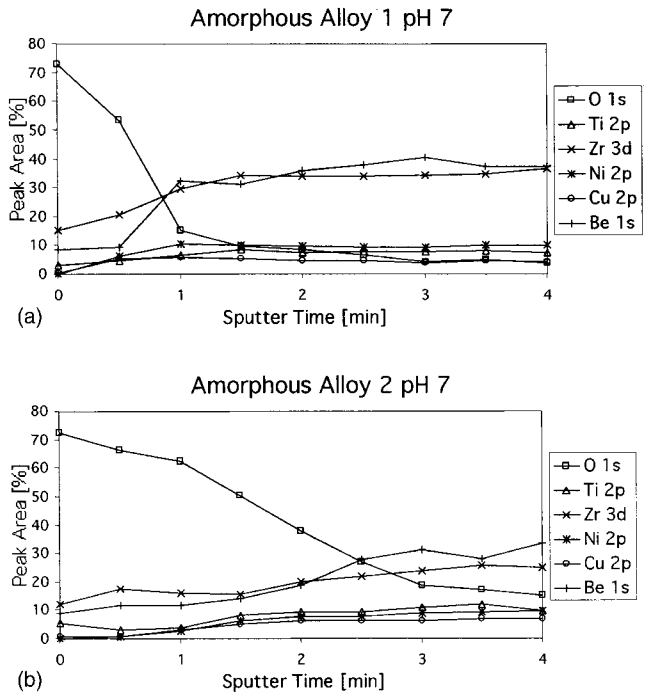

FIG. 4. XPS depth profiles of (a) alloy 1 and (b) alloy 2 after anodic oxidation at *p*H 7.

loys before anodic oxidation show that the outer surface consists mainly of Zr, Be, and Ti in both cases [Figs. 3(a) and 3(b)]. The oxygen signal decreases sharply after 30 s sputter time [Figs. 3(a) and 3(b)] and the metal components reach a value, which stays constant with increasing sputter time. While the oxygen signal disappears in alloy 1 only after 3 min of sputter time [Fig. 3(a)], in alloy 2 it takes only 2 min [Fig. 3(b)]. This might indicate a different oxygen solubility in the bulk for the two alloy compositions. In alloy 1 there is more Zr on the outer surface than Be, but after sputtering they show the same value [Fig. 3(a)]. On the surface no Ni is detected, but after sputtering Ni has the highest value of the three more noble metals [Fig. 3(a)]. Ti and Cu maintain approximately the same ratio from the outer surface to the bulk [Fig. 3(a)]. In alloy 2 the amounts of Zr and Be are the same at the outer surface and after sputtering for 30 s. After 1 min sputter time we see more Be than Zr from the XPS data [Fig. 3(b)]. The three other components reach a constant value after 30 s sputter time with a ratio of Ti>Ni>Cu [Fig. 3(b)], while there is no Ni and only very little Cu on the outer surface. The native oxide in both alloys consists of BeO [Be 1*s* XPS signal is 113 eV, corresponding to Be^{2+} (Ref. 22)], ZrO_y (Zr 3*d* XPS signal is 181.9 and 182.1 eV, corresponding to a nonstoichiometric ZrO_y according to Ref. 23), TiO_2 [Ti 2*p* XPS signal is 458.1 and 458.5 eV, corresponding to Ti^{4+} (Ref. 19)], and a small amount of Cu. The Cu 2*p* signal is very small, but the binding energy around 932.0 eV points to Cu^0, but Cu^+ cannot be ruled out. After a sputter time of 30 s a shift to lower binding energies is observed with all components, consistent with Be^0, Cu^0, Ni^0, Ti^0, and Zr^0. The fact that all metals are in their elemental state, although there is still a small oxygen signal remaining, is an additional indication that the oxygen is dissolved in the bulk close to the surface.

Electrochemical oxidation of the amorphous alloys at *p*H 7 leads to the formation of oxide films, with the oxide film on alloy 1 being thinner than the oxide film on alloy 2 [Figs. 4(a) and 4(b)]. The relative concentrations of the alloy components reach the values of the unoxidized samples after 1 min of sputter time in the case of alloy 1 [Fig. 4(a)] and after 2 min of sputter time for alloy 2 [Fig. 4(b)]. In both cases the Zr seems to be slightly enriched in the oxide film as compared to the unoxidized samples. This could in part be due to anodic dissolution of beryllium and/or titanium hydroxides. The relative concentrations might be affected by preferential sputtering, but as similar values are reached for all elements under all conditions for long sputter times, these effects are probably negligible. The steep decrease in the amount of oxygen in alloy 1 [Fig. 4(a)] suggests that the oxide film ends after 1 min of sputtering. The Zr 3*d* signal from alloy 1 [Fig. 5(A)] shows that after 30 s sputter time Zr^{4+} and Zr^0 are present, while after 1 minute of sputtering only Zr^0 is detected. Similar transitions from the highest oxidation state to the lowest are seen for Be and Ti. Cu and Ni are zero valent as soon as they appear during sputtering. Alloy 2 shows an oxide film that extends further into the bulk. The Zr 3*d* signal corresponding to Zr^{4+} in the depth profile only disappears after 2 min of sputtering [Fig. 5(B)]. But, Zr^0 starts to appear already after 1 min of sputter time. This suggests a gradual change from oxide to bulk alloy. Again, similar transitions from the highest to the lowest oxidation state are found for Be and Ti, while Cu and Ni are zero valent as soon as they appear in the depth profile. In the case of Ti there is evidence for Ti^{3+} and Ti^{2+} in the XPS depth

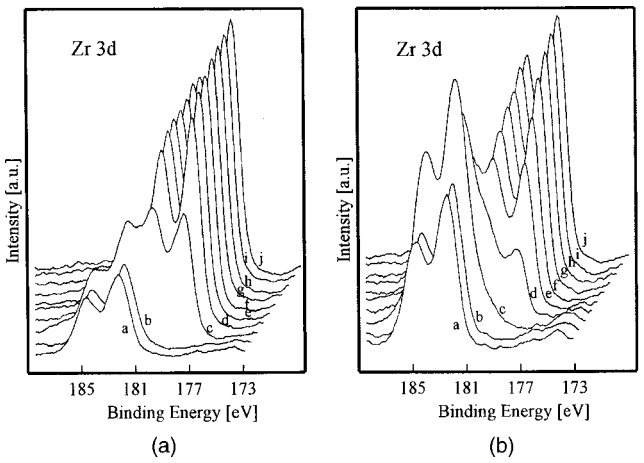

FIG. 5. Zr 3*d* signals during XPS depth profiles of (A) alloy 1 and (B) alloy 2 after anodic oxidation at *p*H 7. (a) and (b) Before sputtering, (c) 0.5 min sputter time, (d) 1.0 min sputter time, (e) 1.5 min sputter time, (f) 2.0 min sputter time, (g) 2.5 min sputter time, (h) 3.0 min sputter time, (i) 3.5 min sputter time, and (j) 4.0 min sputter time.

profile (Fig. 6). This suggests that in both cases the oxide consists of ZrO_2, BeO, and TiO_2 with increasing amounts of Ni, Cu, and lower oxidation states of Ti and zero valent Ti, Zr, and Be with increasing depth. The anodic oxidation also seems to have increased the amount of oxygen dissolved in the bulk, as the oxygen signal does not disappear completely in the depth profiles [Figs. 4(a) and 4(b)].

In acidic solution both alloys show the least corrosion resistance in the electrochemical oxidation (Figs. 1 and 2). The depth profiles after oxidation at *p*H 5 [Figs. 7(a) and 7(b)] show an increased amount of Zr and Ti on the outer surface. This might suggest selective dissolution of BeO at *p*H 5. The thickness of the oxide film seems to be reversed

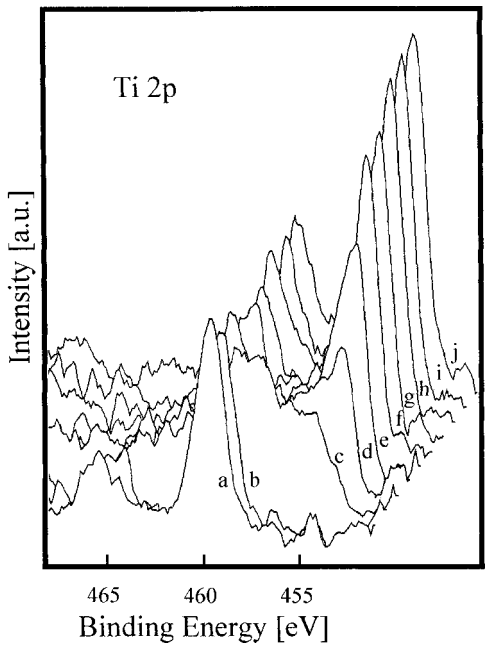

FIG. 6. Ti 2*p* signals during XPS depth profiles of alloy 2 after anodic oxidation at *p*H 7. (a)–(j) are the same as in Fig. 5.

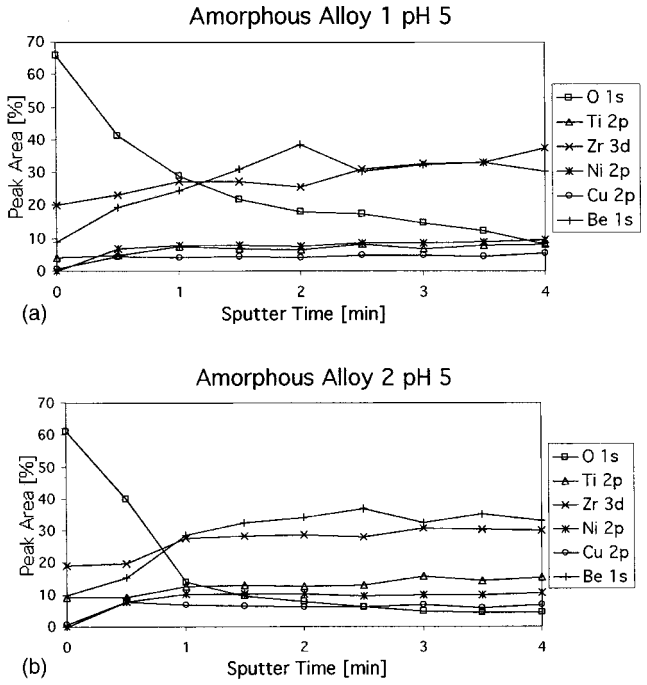

FIG. 7. XPS depth profiles of (a) alloy 1 and (b) alloy 2 after anodic oxidation at *p*H 5.

compared to *p*H 7 [Figs. 4(a) and 4(b)] with alloy 1 showing the thicker oxide than alloy 2 [Figs. 7(a) and 7(b)]. The number of pits is higher in alloy 1 than in alloy 2 (Fig. 2), indicating that the thinner film on alloy 2 is more stable than the thicker oxide film on alloy 1. As alloy 2 has a smaller concentration of Be than alloy 1, it is possible that the difference in pitting is due to anodic dissolution of Be. For both alloys the XPS shows that the outer surface consists of ZrO_2, TiO_2, and BeO with only a little Cu as was the case at *p*H 7. The depth profile from alloy 1 at *p*H 5 [Fig. 7(a)] indicates that the oxide film ends after 1 min of sputtering. The Zr 3*d* and Ti 2*p* spectra change in a similar way as shown in Figs. 5 and 6, confirming the absence of oxidized Zr, Ti, and Be only after sputter times higher than 1 min. Cu and Ni again are zero valent when they appear in the depth profiles. An XPS analysis of only the pit area gave almost the same result as for the rest of the surface except for about a 2/3 decrease in the Be 1*s* signal inside the pit, again pointing to dissolution of BeO. Alloy 2 has a thinner oxide film after oxidation at *p*H 5 [Fig. 7(b)]. In the depth profile the Zr 3*d*, Ti 2*p*, and Be 1*s* signals completely shift to the value of zero valent species after 1 min of sputtering, with only a small amount of oxidized species visible after 30 s sputter time. Cu and Ni are zero valent when they appear in the depth profiles. In both alloys there is oxygen dissolved in the bulk, as the oxygen signal does not disappear during the depth profile [Figs. 7(a) and 7(b)]. Alloy 2 has less pits and XPS analysis inside a pit shows about a 3.5 times increase in the Cu 2*p* signal. The differences of the XPS spectra in the pits from alloys 1 and 2 indicate a different mechanism in pit formation for the two different alloy compositions. Depth profiles inside the pits were not measured, as the very irregular shape

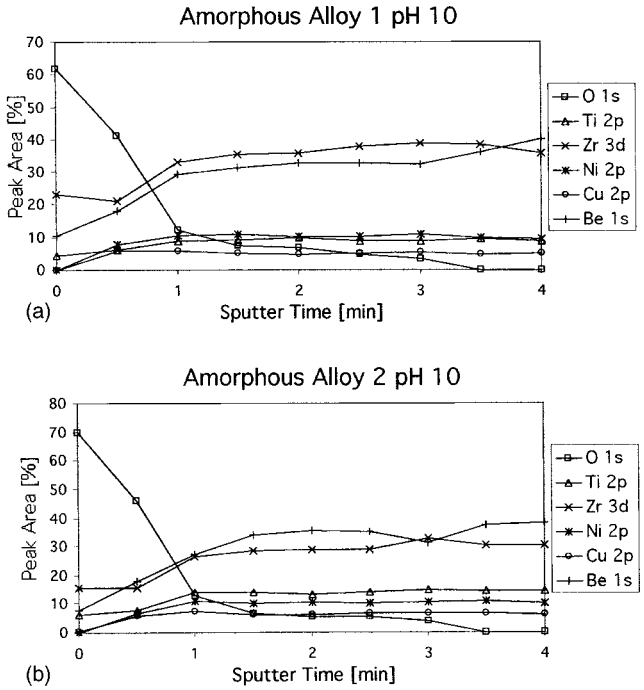

FIG. 8. XPS depth profiles of (a) alloy 1 and (b) alloy 2 after anodic oxidation at *p*H 10.

of the pits and its walls prevent defined layer by layer sputtering and probably lead to preferential sputtering.

In basic solution (*p*H 10) both alloys form similar oxides during electrochemical oxidation. During anodic oxidation no significant differences are detected [Figs. 1(e) and 1(f)]. The XPS depth profiles after oxidation at *p*H 10 are very similar [Figs. 8(a) and 8(b)]. The oxide layer seems to have the same thickness, which is confirmed by the fact that only zero valent Zr, Ti, and Be are detected after 1 min of sputtering. After a sputter time of 30 s the peaks corresponding to the zero valent metals are higher than the peaks corresponding to oxidized species. The oxide film again consists of ZrO_2, TiO_2, and BeO, with Cu and Ni metal only appearing after 30 s of sputtering. The oxygen signal disappears after 3.5 min of sputtering [Figs. 8(a) and 8(b)], as is the case in the reference samples [Figs. 3(a) and 3(b)]. The oxide film formed in *p*H 10 solutions is very similar to the native oxide, except for thickness. There is no evidence of any selective dissolution at this *p*H. The oxide formed at *p*H 10 is approximately twice as thick as the native oxide.

IV. CONCLUSIONS

The native oxide and the oxides formed on amorphous alloys 1 and 2 under mild anodic oxidation conditions follow approximately the predictions of the modified Cabrera Mott model. The model predicts that BeO, ZrO_2, and TiO should form first, according to the free energy at a per mole oxygen basis. We found that the oxides formed at *p*H 5, 7, and 10 mainly consist of ZrO_2, BeO, and TiO_2. The fact that we find more zirconium oxide than beryllium oxide is probably connected with alloy composition, and/or selective dissolution. With the different titanium oxides the prediction which oxide forms is difficult even with binary alloys.[19] Therefore, the model gives a good qualitative approximation on the oxide formed even for amorphous alloys containing five different metals.

The alloys oxidize under all conditions with the least amount of oxide formed at *p*H 10 and severe pitting corrosion at *p*H 5. In basic and neutral solutions the Zr, Ti, and Be oxides form stable passive films as amorphous hydroxides, as has been shown for Zr.[24] As alloy 1 has a higher concentration of Zr and Be it is more resistant to corrosion at *p*H 7. In acidic conditions the Zr, Be, and Ti amorphous hydroxides cannot form leading to a crystalline oxide layer that dissolves readily, showing evidence for selective dissolution of Be. Therefore, alloy 1, which has a higher concentration of Be, shows more severe pitting at *p*H 5. While amorphous metals usually show better corrosion resistance due to the lack of grain boundaries, corrosion is not prevented under all conditions.

ACKNOWLEDGMENTS

Work at Lamar University was supported by the Robert A. Welch Foundation (Houston, TX) under Grant No. V-1103, the Gulf Coast Hazardous Substance Research Center under Grant No. EPA-118LUB, and the Texas Advanced Research (Technology) Program under Grant No. 003581-004. Work at Texas A&M University was supported by the Robert A. Welch Foundation (Houston, TX) under Grant No. A-0514.

[1]M. Yamasaki, H. Habazaki, and K. Hashimoto, J. Electrochem. Soc. **147**, 4502 (2000).
[2]S. Hiromoto, A. P. Tsai, and T. J. Hanawa, Corros. Sci. **42**, 1651 (2000).
[3]V. Schroeder, C. J. Gilbert, and R. O. Ritchie, Scr. Mater. **38**, 1481 (1998).
[4]A. Peker and W. L. Johnson, Appl. Phys. Lett. **63**, 2342 (1993).
[5]A. Inoue, T. Zhang, N. Nishiyama, K. Ohba, and T. Masumoto, Mater. Trans., JIM **34**, 1234 (1993).
[6]Y. He, R. B. Schwarz, and J. I. Archuleta, Appl. Phys. Lett. **69**, 1861 (1996).
[7]C. C. Hays, C. P. Kim, and W. L. Johnson, Appl. Phys. Lett. **75**, 1089 (1999).
[8]C. C. Hays, P. Kim, and W. L. Johnson, Mater. Res. Soc. Symp. Proc. **554**, 243 (1999).
[9]Y. J. Kim, R. Busch, W. L. Johnson, A. J. Rulison, and W. K. Rhim, Appl. Phys. Lett. **65**, 2136 (1994).
[10]T. A. Waniuk, R. Busch, A. Masuhr, and W. L. Johnson, Acta Mater. **46**, 5229 (1998).
[11]S. Schneider, W. L. Johnson, and P. Thiyagarajan, Appl. Phys. Lett. **68**, 493 (1996).
[12]Amorphous Technologies International, 25800 Commerce Center, Ste 100, Lake Forest, CA 92630.
[13]D. L. Cocke, M. S. Owens, and R. B. Wright, Appl. Surf. Sci. **31**, 341 (1988).
[14]D. L. Cocke, G. Liang, M. Owens, D. E. Halverson, and D. G. Naugle, Mater. Sci. Eng. **99**, 497 (1988).
[15]C. Yoon and D. L. Cocke, Appl. Surf. Sci. **31**, 118 (1988).
[16]T. Mebrahtu, T. R. Hess, D. E. Mencer, K. G. Balke, D. G. Naugle, and D. L. Cocke, Mater. Sci. Eng., A **134**, 1041 (1991).
[17]D. L. Cocke, D. G. Naugle, and R. Schennach, in *Materials Science I*, edited by S. Seal, N. B. Dahotre, J. J. Moore, and B. Mishra (The Minerals, Metals, and Materials Society, Warrendale, PA, 2000), p. 23.
[18]D. L. Cocke, S. Promreuk, R. Schennach, M. Y. A. Mollah, and D. G. Naugle, Mater. Res. Soc. Symp. Proc. **574**, 125 (1999).
[19]D. L. Cocke, T. R. Hess, T. Mebrahtu, D. E. Mencer, and D. G. Naugle, Solid State Ionics **43**, 119 (1990).

[20]R. Schennach, S. Promreuk, D. G. Naugle, and D. L. Cocke, Oxidation of Metals (to be published).
[21]CRC *Handbook of Chemistry and Physics*, 63rd ed. edited by R. C. West (Chemical Rubber, Boca Raton, FL, 1982).
[22]C. D. Wagner, W. M. Riggs, L. E. Davis, and J. F. Moulder, in *Handbook of X-Ray Photoelectron Spectroscopy*, edited by G. E. Muilenberg (Perkin Elmer, Eden Prairie, MN, 1979).
[23]Y. S. Li, P. C. Wong, and K. A. R. Mitchell, Appl. Surf. Sci. **89**, 263 (1995).
[24]R. Schennach, A. Mamun, N. Kunamneni, and D. L. Cocke, J. Vac. Sci. Technol. A **18**, 1478 (2000).